Local statistics of laminar expanding flames subjected to Darrieus–Landau instability

Zirui Liu^a, Vishnu R. Unni^b, Swetaprovo Chaudhuri^c, Chung K. Law^a, Abhishek Saha^{b,*}

a Department of Mechanical and Aerospace Engineering, Princeton University, Princeton, NJ 08544, USA
 b Department of Mechanical and Aerospace Engineering, University of California San Diego, La Jolla, CA 92093, USA
 c Institute for Aerospace Studies, University of Toronto, Toronto, ON M3H5T6, Canada

Abstract

We, herein, report an experimental study to investigate the role of local flamefront dynamics on the propagation and acceleration of cellularly unstable premixed expanding laminar flames. Using simultaneous Miescattering imaging and Particle Image Velocimetry, we measured the flame edge location and its adjacent flow field, which were subsequently processed to quantify the evolution of the probability density functions (pdfs) of flow velocities, curvature, normal strain rate and tangential strain rate. We showed that appropriate normalization of the measured quantities can unify the data from different pressures when identified with the corresponding Peclet number, defined as the ratio of the flame radius to the flame thickness. Since the flamefront is stable and smooth at lower Peclet numbers, the flame-induced flow field and stretch rates are almost uniform over the flamefront, resulting in narrow pdfs. At higher Peclet numbers, however, the flame becomes progressively more wrinkled and hence the variations in the local quantities increase leading to wider pdfs. Furthermore, while the mean curvature was found to be inversely proportional to the mean flame radius and insensitive to the cellular structure, the mean normal strain rate was strongly influenced by the cellular structure.

Keywords: Darrieus-Landau instability; Stretch rate; Curvature

1. Introduction

The structure and propagation of laminar flames can be subjected to intrinsic cellular flamefront instability which wrinkles the otherwise

* Corresponding author.

E-mail address: asaha@eng.ucsd.edu (A. Saha).

smooth flamefront through the emergence of cells. The continuous generation and evolution of the cells augment the flame surface area and hence the flame burning rate, leading to *self-acceleration*, a state at which the flame accelerates without any external agent. Cellular instability in laminar flames can manifest in two modes, namely, Darrieus-Landau (DL) hydrodynamic instability, induced by a sharp density gradient across the flamefront; and

diffusional-thermal (DT) instability, triggered in mixtures with sub-unity Lewis numbers, *Le* (defined as the ratio of thermal diffusivity of the mixture to mass diffusivity of the deficient species). For these two modes of cellular instability, the former is of particular relevance for internal combustion engines, which operate at high pressures, and hence promote the DL instability through reduced flame thickness.

Following Darrieus [1] and Landau [2], Sivashinsky, Matalon and co-workers [3-9] further analyzed the onset of the DL instability, the dynamics of cellular structure, growth rate and cut-off limits of cells, using both linear and nonlinear methods. In numerical studies, a major focus has been on the onset and development of the cellular structure [10-12]. Experimentally, the development of cellular structure and its role in flame propagation has been studied on both planar unstretched [13,14] and stretched expanding flames [15-18]. Bradley et al. [19] and Bauwens et al. [20,21] used large scale atmospheric expanding flames to identify key features of DL instability, however, with possible influence of buoyancy. To facilitate the development of DL instability while minimizing the influence of buoyancy, Law and co-workers [16,17] utilized a constant and high-pressure chamber to study small-scale expanding flames at elevated pressures. These works collectively established that the cellularly unstable expanding flames, indeed, exhibit self-acceleration once the flame becomes larger than a critical radius [22,23]. Some of the studies have also assessed the acceleration exponent by establishing a fractal based scaling model [24-26]. More recently Yang et al. [17] demonstrated that the propagation of cellularly unstable flames from the same mixture at varying pressures can be unified if the propagation speed, $S_L = dR_f/dt$, normalized by the laminar planar flame speed $S_{L,0}$ is plotted with flame radius, R_f normalized by laminar planar flame thickness, $\delta_{L,0}$, or the Peclet number, $Pe = R_f/\delta_{L,0}$. Based on this normalization, they have also identified three characteristically different stages of propagation. Specifically, at *smooth expansion stage* corresponding to low Pe, the flame surface is smooth and devoid of a cellular structure. In the transition stage with Pe larger than a critical value, Pe_{cl} , cellular structure starts appearing over the flame surface and the flame starts accelerating. Finally, at large Pe_{c2} or the saturated stage, the cellular structure covers the entire flamefront and the propagation has a constant acceleration exponent [17], which was found to be less than 1.5, for a wide range of mixtures. It has been suggested [16,20,27,28] that this particular value of 1.5 is believed to indicate that the flame has assumed the characteristics of a turbulent flame, and the transformation has been termed self-turbulization.

The above review shows that practically all the experimental studies of the cellularly unstable ex-

panding flames were on the global flame behavior. It is, however, obvious that local flamefront dynamics is critical in governing the flame acceleration, as shown for example in many studies on turbulent flames [29–32]. For our present problem, it is reasonable to expect that a cellularly unstable laminar flamefront and its irregular cellular structure can induce a non-uniform flow pattern ahead of the flamefront, which in turn can affect the flame propagation. Furthermore, similar to turbulent flames, the broadband flow non-uniformity arising from the cellular structure of various length scales can also strain and wrinkle flamefronts, which may cause additional acceleration.

In response to the above considerations, we have conducted a systematic study on the effect of DL cellular structure on the local flow and the flame-front. Using diffusionally neutral mixtures ($Le \approx 1$) at elevated pressures, we have isolated the effects of DL instability and quantitatively measured the flow field and stretch rates conditioned at wrinkled flamefront. Their relative strengths, evolution with flame size and pressure have been identified and discussed. The results are reported in the following sections.

2. Methodology

2.1. Experimental specifications

Experiments were conducted in our well-vetted dual-chamber vessel, in which propagation of the centrally spark-ignited expanding flame can be studied in a constant pressure environment. The details of the chamber can be found in our previous publications [33,34] and the Supplementary Material. Diffusionally neutral ($Le \approx 1$) $H_2/O_2/N_2$ mixtures at stoichiometric condition were selected for this study to alleviate possible stabilizing or destabilizing effects of the DT instability and prevent interference from any other types of intrinsic instability. Experiments were conducted at pressures ranging from 1 to 10 atm. Two different dilution ratios $(N_2/(N_2 + O_2)\%)$ were studied to assess the effect of flame temperature (T_f) or thermal expansion ratio, $\Theta = T_f/T_u$, where T_u is the unburned gas temperature. The conditions are tabulated in Supplementary Material.

Mie scattering images and high speed 2D-Particle Image Velocimetry (PIV) were jointly used to measure the instantaneous flow velocity and flamefront geometry. Before each experimental run, the chamber was filled with required proportion of gas mixture which was seeded with DEHS droplets (nominal diameter $1-2~\mu m$) generated by an airblast nebulizer. A high speed dual-head Nd-YLF laser (527 nm) along with turning mirrors and sheet making optics was used to generate laser sheet which was sent inside the chamber through a small optical window. The energy per pulse at 8kHz

repetition rate was 3.3 mJ and the thickness of the laser sheet at the center of the chamber was approximately 800 μ m. A high-speed camera (Phantom v12.1) located orthogonal to the laser plane was synchronized with the laser pulses to record the event at 16,000 fps with a window size of 560×552 pixel² to achieve a spatial resolution of 0.07mm/pixel.

Before ignition, the seeding droplets are uniformly distributed. After spark ignition at the center of the inner chamber, the flame starts to propagate outwardly and vaporize the droplets on the burned side, limiting the high seeding density only on the unburned side. We recognize that the flame edge identified with this technique is an isotherm corresponding to the boiling point of the DEHS, which changes with pressure. However, for the range of pressure (1–10 atm) reported in this study, the boiling point of the seeding droplets changes only by 80K (from 638K to 718K), which is significantly less compared to the temperature rise across the flamefront, and as such its effect on the detected flamefront at various pressure is expected to be small. The Mie scattering images are processed using DaVis 8.0 (Lavision) to generate vector field with a resolution of 0.5mm/vector, while the edge detection is completed by MATLAB Canny edge detection algorithm. The estimated uncertainty of the velocity measurement is about $\pm -2\%$ [35], while that for the edge detection is around +/-1%. The mean radius of the flame is calculated as $R_f =$ $\sqrt{A/\pi}$, where A is the area enclosed by the flame edge, and the flame speed, S_L is determined from the relation $S_L = dR_f/dt$. To avoid the ignition and wall effects, only data within the range 5mm < $R_f < 20$ mm are used, which is 30% of the chamber size. Each experimental condition was repeated several times to obtain converged statistics of the quantities reported.

2.2. Computational specifications

Fundamental properties, such as laminar unstretched flame speed $S_{L,0}$, adiabatic flame temperature T_f and flame thickness $\delta_{L,0}$ are calculated using CHEMKIN 1-D flame solver and kinetics model of Burke et al. [36]. In this study, we used diffusive flame thickness, defined as $\delta_{L,0} = D/S_{L,0}$, where D is the thermal diffusivity of the mixture.

3. Results and discussion

We now present and discuss the evolution of local flamefront statistics observed due to the cellular structure of DL instability on expanding laminar flames. In particular, we will focus on the evolution of flow statistics and local stretch rates, in the three stages of propagation mentioned in Section. 1. We will first focus on the experiments at $T_f=1800\mathrm{K}$ to analyze the local dynamics and the evolution of

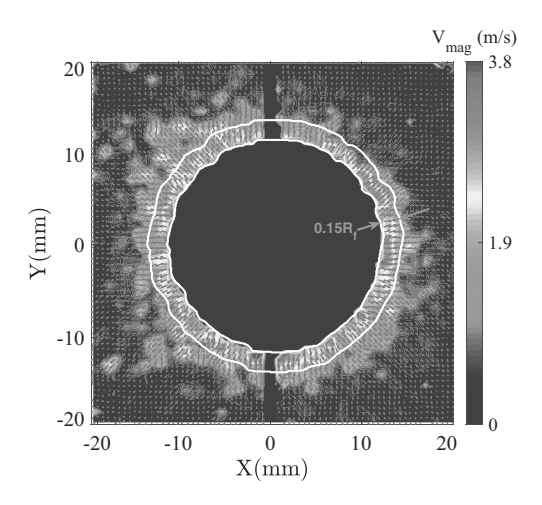


Fig. 1. Velocity field induced by the laminar cellularly-unstable expanding flame in the unburned side. $T_f = 1800 \text{K}$, P = 10 atm.

statistics at various pressures. The effect of flame temperature will subsequently be discussed in a separate subsection. We note that in the following discussion, a normalized quantity has been identified with an overhead line $(\overline{})$, while ensemble average of a quantity is denoted by a triangle bracket $(<\cdot>)$.

3.1. Statistics of flow velocity

The flame in our experiment expands in a quiescent environment, and hence we are mostly interested in the flame-generated flow, which is localized just adjacent to the flamefront in the unburned side (shown in Fig. 1). Thus, we confined our velocity analysis in a zone of a thickness of $0.15R_f$ next to the flamefront (See Supplementary Materials for details). Since we are discussing the effect of DL instability in a spherically expanding flame, which is best described in the polar co-ordinate system $(r - \theta)$, we performed our analysis on radial (V_r) and angular (V_θ) components of velocity, measured at different stages of flame propagation.

Fig. 2(a) shows the probability density function (pdf) of normalized radial velocity, $\overline{V_r} = V_r/S_{L,0}$, measured adjacent to the flamefront for three different flame sizes $(R_f s)$ at different pressures for $T_f = 1800 \text{K}$. It is seen that, at 1 atm, the pdf s for all three R_f are narrow and almost identical. The flamefront at this pressure is smooth and devoid of any cellular structure $(smooth\ expansion\ stage)$. The propagation speed for the unity $Le\ mixture$ is constant with the flame size or stretch rate and hence, there is no acceleration. Furthermore, all the three pdf s have peaks at 4.5, which is close to the analytically estimated normalized radial flow

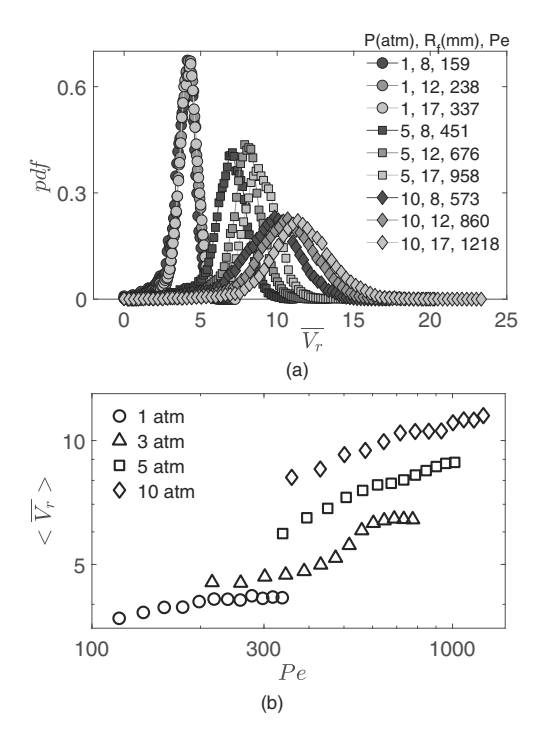


Fig. 2. Normalized radial velocity, V_r/S_{L0} , ahead of the flame under 1, 5, 10atm ($T_f = 1800$ K), (a) pdf. (b) mean.

velocity $(\overline{V_r})$ for a radially expanding smooth flame [37], $\Theta - 1 \approx 5$.

At higher pressures, such as 5 and 10atm, the cells start to appear and grow on the flamefront causing the flame to accelerate, and eventually lead to the saturation stage. In such situation, the peaks (and the mean) of the pdfs shift to larger values as the flame expands. It is also noticed that the normalized velocity pdfs have wider distributions at higher pressures caused by the reduction in the laminar flame speed. The mean of the normalized radial flow velocity, $\langle \overline{V_r} \rangle$, at various pressures is plotted as function of Pe in Fig. 2(b), which displays three distinct slopes, corresponding to three stages of propagation, previously determined based on the global propagation speed [17]. The boundaries of these three stages are found to be around Pe = 400 and Pe = 700, which are also consistent with the result in [17].

The pdfs of normalized angular velocity $(\overline{V_{\theta}})$, shown in Fig. 3, display similar behavior, in that at 1 atm, the pdfs are narrower for different $R_f s$, while for higher pressures, they become progressively wider. Since the mean flame propagation is predominantly in the radial (r) direction, and the local non-zero V_{θ} arises from mis-alignment between the radial and the flame-normal directions, the mean of the V_{θ} pdfs are expected to be negligible, which is reflected in the pdfs which are symmetric about $\overline{V_{\theta}} = 0$ value.

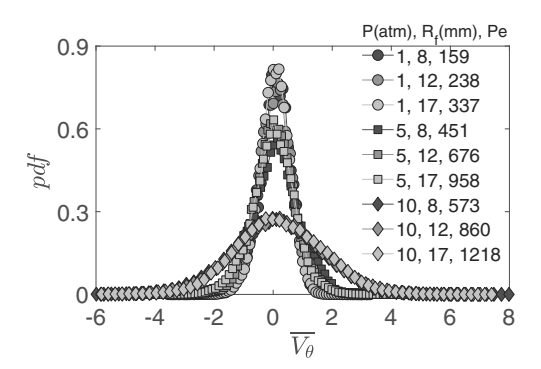


Fig. 3. Normalized angular velocity ahead of the flame under 1, 5, 10atm ($T_f = 1800$ K).

3.2. Statistics of curvature

Next we analyze the statistics of local curvature (κ) , whose variation on cellularly unstable flamefront is representative of scales of cellular structures. Since for a smooth stable spherically expanding flame, the local curvature is unique and inversely proportional to the flame radius (R_f) , we define the normalize curvature as, $\overline{\kappa} = \kappa \times R_f$. Fig. 4(a) compares the pdfs of $\overline{\kappa}$ at various pressures and Pe for flames with $T_f = 1800$ K. For low Pes, where the flames are still stable and devoid of cellular structures, variation in the local curvature is minimal, and hence, the pdfs are narrower. They, however, become wider as Pe increases, due to development of the DL cellular structure. With increase in Pe, the flames become progressively wrinkled resulting in wider distributions. It is also noted that the pdfs are asymmetric around its peak value particularly for higher Pe. This is an artifact of Huygens' propagation, in which the extent of negatively curved section of a randomly wrinkled freely propagating surface progressively reduces with time, and hence reduced negative local curvature. The mean, $\langle \overline{\kappa} \rangle$, is independent of Pe and close to unity (Fig. 4(b)) affirming $<\kappa>\approx 1/R_f$. We further note that pdfs and mean of $\overline{\kappa}$ at similar Pes, arising from different combinations of pressure and R_f , are similar. This confirms that the proposed normalization unifies the effects of R_f and pressure properly. The standard deviation of the *pdfs*, which is a measure of its width, is found to be almost constant at small Pe (smooth propagation stage) and increases monotonically after the critical value when the flame becomes cellularly unstable (Fig. 4(b)). Furthermore, between transition stage and saturation stage, we do not see discernible changes in the slope. This is due to the fact that the maximum and minimum values of $<\bar{\kappa}>$, bounded by the cut-off limit and flame size respectively, are both independent of the propagation speed.

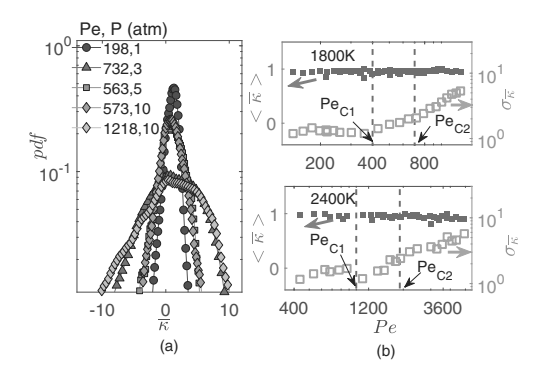


Fig. 4. (a) Pdfs of curvature ($\overline{\kappa}$) at different Pe for $T_f=1800$ K. The estimated uncertainty in the measured curvature is around \pm 5%. (b) Mean normalized curvature, $<\overline{\kappa}>$ (left y-axis), and standard deviation, $\sigma_{\overline{\kappa}}$ (right y-axis), as function of Pe for $T_f=1800$ K (top row) and 2400 K (bottom row). The vertical lines represent the two transitional critical Peclet numbers. Transition from 1st to 2nd stage, $Pe_{c1}=400$ ($T_f=1800$ K) and 1000 ($T_f=2400$ K). Transition from 2nd to 3rd stage, $Pe_{c2}=700$ ($T_f=1800$ K) and 1900 ($T_f=2400$ K).

3.3. Statistics of stretch rates

Next, we analyze the effect of instability on the local stretch rate defined in general as the fractional rate of change in the area (A) of a Lagrangian element of the flame surface, $\mathbf{K} = (1/A)(dA/dt)$. Hydrodynamic theory shows that the total stretch rate can be decomposed into three components [38] namely, (1) stretch by pure curvature (\mathbf{K}_c)

which measures the effect of the normal propagation of a curved flame surface; (2) normal strain (\mathbf{K}_n) , which measures the effect of the non-uniformity in normal velocity near the curved flame surface, and (3) tangential strain (\mathbf{K}_t) , which measures the compression or expansion effect of tangential velocity on the flamefront. These three components can be mathematically expressed as [39]

$$\mathbf{K} = \underbrace{S_d \kappa}_{\mathbf{K}_c} + \underbrace{(-\mathbf{v} \cdot \mathbf{n}) \kappa}_{\mathbf{K}_n} + \underbrace{\nabla_t \cdot \mathbf{v}_t}_{\mathbf{K}_c}$$
(1)

where, S_d is the local stretched displacement speed, which is equivalent to $S_{L,0}$ for unity Lewis number flames, such as ours. It is noted that in our definition, the flame-normal vector, n, points towards the burned side. Furthermore, following the discussion of normalization of curvature, we also recognize that the stretch rates for cellularly unstable expanding flame can be normalized by multiplying $R_f/S_{L,0}$. Since we have already discussed evolution of the statistics of $\overline{\mathbf{k}}$, which is equivalent to $\overline{\mathbf{K}}_c$, we now discuss the statistics of $\overline{\mathbf{K}_n} = \mathbf{K}_n \times (R_f/S_{L,0})$ (Fig. 5(a)) and $\overline{\mathbf{K}}_t = \mathbf{K}_t \times (R_f/S_{L,0})$ (Fig. 6(a)). In general, their statistics display similar behavior with that of $\overline{\kappa}$, in that the *pdf*s are initially narrower at lower Pe, when the flamefront is stable and smooth, and subsequently becomes wider with increasing Pe, as the flame becomes progressively more wrinkled due to the DL instability. As Pe increases, the range of cell sizes for spherically expanding flames with DL instability also increases [9]. A wider range of scales for cellular structure, will in turn induce a wider range of non-uniformity

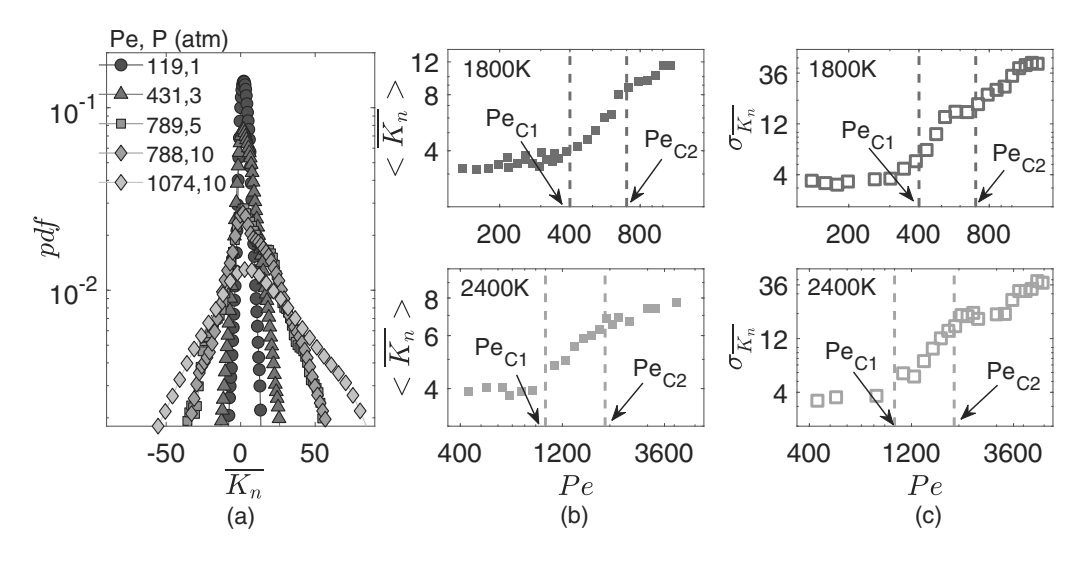


Fig. 5. (a) Pdfs of normalized normal strain rate $(\overline{\mathbf{K}_n})$ at different Pe for $T_f=1800$ K. The uncertainty is around $\pm 9\%$. (b) Mean normalized normal strain rate, $<\overline{\mathbf{K}_n}>$, as function of Pe for $T_f=1800$ K and 2400K. (c) Standard deviation of the normalized normal strain rate, $\sigma_{\overline{\mathbf{K}_n}}$, as function of Pe for $T_f=1800$ K and 2400K. The vertical lines represent critical Peclet numbers as described in Fig. 4.

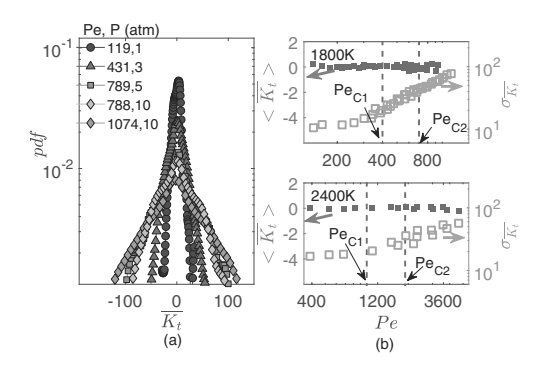


Fig. 6. (a) Pdfs of normalized tangential strain rate $(\overline{\mathbf{K}_t})$ at different Pe for $T_f = 1800$ K. The uncertainty is around \pm 5%.(b) Mean normalized tangential strain rate, $<\overline{\mathbf{K}_t}>$, and standard deviation, $\sigma_{\overline{\mathbf{K}_t}}$, as function of Pe for $T_f = 1800$ K and 2400K. The vertical lines represent critical Peclet numbers as described in Fig. 4.

in the (flame-generated) flow, which causes broadening effect in the pdfs of $\overline{\mathbf{K}}_n$ and $\overline{\mathbf{K}}_i$.

It is to be noted that the mean of the normalized normal strain, $\langle \overline{\mathbf{K}_n} \rangle$, exhibits three different slopes at the three stages (Fig. 5(b)), a behavior also observed for the propagation speed. \mathbf{K}_n includes effects of both curvature, κ and non-uniformity of flow in the normal direction, $(-\mathbf{v} \cdot \mathbf{n})$, as shown in Eq. (1). For expanding flames, the mean curvature is inversely proportional to the flame size, < $\overline{\kappa} > \approx 1$ for both stable (low *Pe*) and unstable (high Pe) flames (Fig. 4(b)). On the other hand, $(-\mathbf{v} \cdot \mathbf{n})$, which is the flow velocity in the normal direction of the flamefront, is driven by the flame propagation and as a result, should be strongly correlated with the flame propagation speed. Therefore, the three-stage behavior of $\langle \overline{\mathbf{K}_n} \rangle$ is the combined effect of the three-stage behavior of the propagation speed and the almost constant mean curvature $<\overline{\kappa}>$. Interestingly, the standard deviation of $\overline{\mathbf{K}_n}$, which quantifies the width of the pdf, also displays a three-stage behavior as shown in (Fig. 5(c)) owing to its direct relation with the propagation speed.

The mean of normalized tangential strain, $< \overline{\mathbf{K}_t} >$, however, remains close to zero (Fig. 6(b)), since the local tangential strain rate due to the flame-generated flow can be both equally positive and negative. The standard deviation, on the other hand, stays almost constant for smooth flames at low Pe and increases monotonically after the onset of instability (high Pe) due to the augmented variation in the angular alignment between flame-normal direction and flow vector (Fig. 6(b)). Since the tangential strain is not directly related to the flame propagation, it does not exhibit a three-stage behavior.

Although with Pe, pdfs of all three stretch rates become wider, it is worth noting that, at a fixed Pe, $\overline{\mathbf{K}}_t$ shows the most broadband distribution, while

pdf of $\overline{\mathbf{K}}_c$ is the narrowest. Furthermore, if we look at the mean total stretch rate, i.e. $<\overline{\mathbf{K}}>=<\overline{\mathbf{K}}_c>+<\overline{\mathbf{K}}_n>+<\overline{\mathbf{K}}_t>$, the contribution from $<\overline{\mathbf{K}}_n>$ is more than 70%, while that from $<\overline{\mathbf{K}}_t>$ is almost negligible.

3.4. Joint distribution of stretch rates

While the previous analysis of the pdfs of stretch rates shows their individual statistics, for cellularly unstable flame propagating in a quiescent environment, their evolution is an outcome of the interplay between the dynamics of local cellular structures and non-uniformity in flame-generated flow. In other words, \mathbf{K}_c , \mathbf{K}_n and \mathbf{K}_t do not evolve independently and as such, we next discuss the joint probability density functions (jpdfs) of these stretch rates, which illustrates their effects on each others' statistics. In particular we recognize that the shapes of the *ipdf*s of two quantities, say O1 and O2, can be used to interpret the range of possible values of O1, for a fixed value of O2 and vice-versa. Fig. 7(a)–(c) show the *jpdf*s of $\overline{\mathbf{K}}_t$ and $\overline{\mathbf{K}}_n$ for three different values of Pe, corresponding to smooth expansion, transition and saturated stages of flame propagation. Although the x and y axes scales of these three subfigures are different, the aspect ratios (ratio of spans of x and y axes) are kept constant, and hence, the change of the shape of *jpdf*s can be readily assessed. It is seen that as we move from low to high Pe, implying progressively more wrinkled flamefront, the shape of the *jpdf* elongates more in the dimension of $\overline{\mathbf{K}_n}$ than $\overline{\mathbf{K}_t}$. This suggests faster broadening of the pdf of the former compared to the latter, which was also evident from the standard deviation of individual pdfs (Figs. 5(c) and 6(b)). The shape of the *jpdf* also confirms that local values of $\overline{\mathbf{K}_t}$ and $\overline{\mathbf{K}_n}$ could be of the same or opposite signs.

The shape of the *jpdf*'s for normalized $\overline{\mathbf{K}_n}$ and $\overline{\mathbf{K}_c}$ resembles a unique diagonal patch (Fig. 7(d)–(f)), signifying positive correlation and that locally they are mostly of both either positive or negative. Furthermore, the ratio of $\overline{\mathbf{K}_n}$ and $\overline{\mathbf{K}_c}$ is the measure of flame induced flow velocity (Eq. (1)), which increases strongly with flame wrinkling due to cellular instability, and hence Pe. This is why the slope of the diagonal patch increases and it becomes more aligned with the axis of $\overline{\mathbf{K}_n}$, as we move to higher Pe (Fig. 7(d)–(f)).

3.5. Effects of flame temperature

To assess the role of flame temperature or thermal expansion on the measured statistics, we have also studied $H_2/O_2/N_2$ flames with $T_f = 2400$ K at various pressures. At $T_f = 2400$ K, $\overline{\mathbf{K}}_c$, $\overline{\mathbf{K}}_n$ and $\overline{\mathbf{K}}_t$ qualitatively resemble the characteristics of data at $T_f = 1800$ K, in that pdfs become wider with

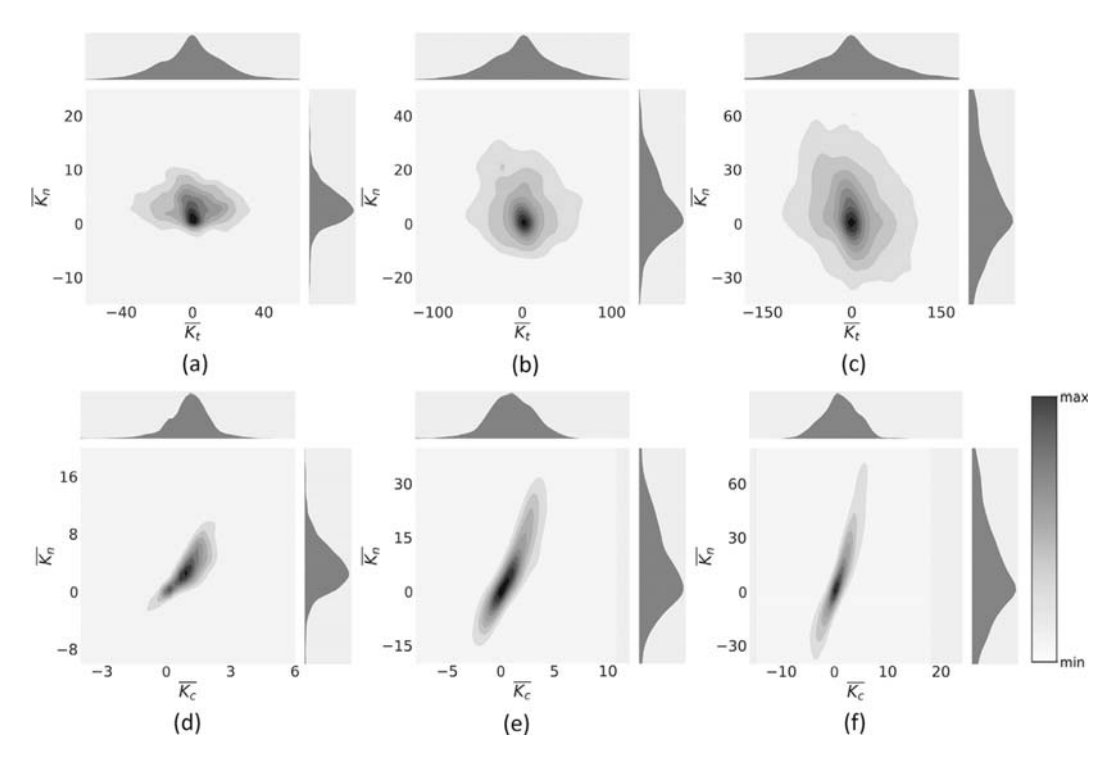


Fig. 7. Joint probability distributions. (a)–(c): normalized tangential and normal strain rates, (d)–(f): normalized normal strain rate and stretch by pure curvature. (a) and (d): Pe = 238; (b) and (e): Pe = 676; (c) and (f): Pe = 1074 (Pe = 1074).

increasing Pe due to the emergence of the cellular structure and the increase in local strain. All pdfs are shown in Supplementary Material. The means and standard deviations of $\overline{\mathbf{K}}_c$, $\overline{\mathbf{K}}_n$ and $\overline{\mathbf{K}}_t$ are shown and compared with $T_f = 1800 \mathrm{K}$ in Figs. 4(b), 5(b),(c) and 6(b), respectively. $\langle \overline{\mathbf{K}}_c \rangle$ and $\langle \overline{\mathbf{K}}_t \rangle$ are found to show identical behavior for both $T_f = 1800 \mathrm{K}$ and 2400K. $\langle \overline{\mathbf{K}}_n \rangle$ shows three-stage behavior as well. All three standard deviations also exhibit similar trends with $T_f = 1800 \mathrm{K}$.

4. Conclusions

In summary, in this work we studied local flow and stretch rate statistics of DL-cellularly unstable expanding laminar flames for the first time to our knowledge. Using simultaneous Mie scattering images and high speed PIV, we measured the location of the flamefront and the flow velocities in the unburned region, as the flame propagates. Statistical analysis was performed on the measured local radial and angular velocities, curvature of flamefront, and stretch rates due to normal and tangential strain for different stages of propagation.

At $Pe < Pe_{cl}$, the flame is cellularly stable and thus the flame induced flow adjacent to the flame-front is independent of the flame size, and hence,

the *pdf*'s are fixed and narrow. At higher *Pe*, cellular structures due to DL instability on the flamefront becomes increasingly dominant, promoting the local non-uniformity of the flow, and hence leading to broadened *pdf*'s for both radial and angular velocities

The normalized stretch rates compared over a large range of pressures and flame sizes, show similar behavior in that at low Pe, pdfs are relatively narrower, while at higher Pe, they are progressively wider. Due to the overall spherical geometry, the mean normalized curvature remains unity with Pe, while the mean of the normalized stretch rate due to the tangential strain is almost zero for a large range of Pe. On the other hand, the mean of the stretch rate due to the normal strain displays threestage behavior similar to the flame propagation speed because of the strong correlation between flame propagation speed and flow normal velocity. Experimentation with multiple mixtures with multiple flame temperatures showed weak influence on the statistics of appropriately normalized flow velocity and normalized stretch rates.

Declaration of Competing Interest

None.

Acknowledgments

This work was supported by the US National Science Foundation (CBET, grant no. 1827287).

References

- [1] G. Darrieus, Tech. Mod. 30 (1938) 18.
- [2] L.D. Landau, *Acta Physicochim. URSS* 19 (1) (1944) 77–85.
- [3] G.I. Sivashinsky, Combust. Sci. Technol. 15 (3–4) (1977) 137–145.
- [4] G.I. Sivashinsky, Ann. Rev. Fluid Mech. 15 (1) (1983) 179–199.
- [5] G.I. Sivashinsky, Proc. Combust. Inst. 29 (2) (2002) 1737–1761.
- [6] R. Addabbo, J.K. Bechtold, M. Matalon, Proc. Combust. Inst. 29 (2) (2002) 1527–1535.
- [7] J.K. Bechtold, C. Cui, M. Matalon, *Proc. Combust. Inst.* 30 (1) (2005) 177–184.
- [8] J.K. Bechtold, M. Matalon, *Combust. Flame* 67 (1) (1987) 77–90.
- [9] M. Matalon, Ann. Rev. Fluid Mech. 39 (2007) 163–191.
- [10] F. Creta, M. Matalon, Proc. Combust. Inst. 33 (1) (2011) 1087–1094.
- [11] C. Altantzis, C.E. Frouzakis, A.G. Tomboulides, M. Matalon, K. Boulouchos, J. Fluid Mech. 700 (2012) 329–361.
- [12] R. Yu, X.S. Bai, V. Bychkov, Phys. Rev. E 92 (6) (2015) 063028.
- [13] C. Clanet, G. Searby, *Phys. Rev. Lett.* 80 (17) (1998)
- [14] J.F. Yu, R. Yu, X.Q. Fan, M. Christensen, A.A. Konnov, X.S. Bai, *Combust. Flame* 160 (7) (2013) 1276–1286.
- [15] D. Bradley, Philos. Trans. R. Soc. A 357 (1764) (1999) 3567–3581.
- [16] F. Wu, G. Jomaas, C.K. Law, Proc. Combust. Inst. 34 (1) (2013) 937–945.

- [17] S. Yang, A. Saha, F. Wu, C.K. Law, Combust. Flame 171 (2016) 112–118.
- [18] J. Beeckmann, R. Hesse, S. Kruse, A. Berens, N. Peters, H. Pitsch, M. Matalon, *Proc. Combust. Inst.* 36 (1) (2017) 1531–1538.
- [19] D. Bradley, T.M. Cresswell, J.S. Puttock, Combust. Flame 124 (4) (2001) 551–559.
- [20] C.R. Bauwens, J.M. Bergthorson, S.B. Dorofeev, *Proc. Combust. Inst.* 35 (2) (2015) 2059–2066.
- [21] C.R. Bauwens, J.M. Bergthorson, S.B. Dorofeev, Int. J. Hydrogen Energy 42 (11) (2017) 7691–7697.
- [22] C.K. Law, G. Jomaas, J.K. Bechtold, Proc. Combust. Inst. 30 (2005) 159–167.
- [23] M.Z. Haq, J. Heat Transf. 127 (12) (2005) 1410–1415.
- [24] D. Bradley, T.M. Cresswell, J.S. Puttock, Combust. Flame 124 (4) (2001) 551–559.
- [25] W.K. Kim, T. Mogi, K. Kuwana, R. Dobashi, Proc. Combust. Inst. 35 (2) (2015) 2051–2058.
- [26] F. Wu, G. Jomaas, C.K. Law, Proc. Combust. Inst. 34 (1) (2013) 937–945.
- [27] Y.A. Gostintsev, A.G. Istratov, Y.V. Shulenin, Combust. Explos. Shock Waves 24 (5) (1988) 563–569.
- [28] Y. Xie, J. Wang, X. Cai, Z. Huang, Int. J. Hydrogen Energy 41 (40) (2016) 18250–18258.
- [29] D. Bradley, C.G.W. Sheppart, R. Woolley, D.A. Greenhalgh, R.D. Lockett 122 (1–2) (2000) 195–209, doi:10.1016/S0010-2180(00)00113-9.
- [30] A.M. Steinberg, J.F. Driscoll, S.L. Ceccio, Proc. Combust. Inst. 32 (2) (2009) 1713–1721.
- [31] R. Lamioni, P.E. Lapenna, G. Troiani, F. Creta, Flow Turbul. Combust. 101 (4) (2018) 1137–1155.
- [32] N. Fogla, F. Creta, M. Matalon, Proc. Combust. Inst. 34 (1) (2013) 1509–1517.
- [33] A.P. Kelley, A.J. Smallbone, D.L. Zhu, C.K. Law, *Proc. Combust. Inst.* 33 (1) (2011) 963–970.
- [34] S. Chaudhuri, A. Saha, C.K. Law, Proc. Combust. Inst. 35 (2) (2015) 1331–1339.
- [35] S. Bhattacharya, J.J. Charonko, P.P. Vlachos, *Measur. Sci. Technol.* 29 (11) (2018) 115301.
- [36] M.P. Burke, M. Chaos, Y. Ju, F.L. Dryer, S.J. Klippenstein, Int. J. Chem. Kinet. 44 (7) (2012) 444–474.
- [37] N. Peters, Turbulent Combustion, Cambridge University Press, 2000.
- [38] M. Matalon, B. Matkowsky, J. Fluid Mech. 124 (1982) 239–259.
- [39] M. Matalon, C. Cui, J.K. Bechtold, J. Fluid Mech. 487 (2003) 179–210.